

# Fabrication and Characterization of Three-dimensional Functional Scaffolds for Skin Tissue Engineering



Thesis submitted in partial fulfilment for the  
Award of Degree

**Doctor of Philosophy**

by

*Neelima Varshney*

SCHOOL OF BIOMEDICAL ENGINEERING  
INDIAN INSTITUTE OF TECHNOLOGY  
(BANARAS HINDU UNIVERSITY)  
VARANASI – 221005  
INDIA.

Roll No. 16021002

2022

## CERTIFICATE

It is certified that the work contained in the thesis titled "*Fabrication and Characterization of Three-dimensional Functional Scaffolds for Skin Tissue Engineering*" by "*Neelima Varshney*" has been carried out under my supervision and that this work has not been submitted elsewhere for a degree.

It is further certified that the student has fulfilled all the requirements of Comprehensive Examination, Candidacy and SOTA for the award of Ph.D. Degree.



(Dr. Sanjeev Kumar Mahto)

18.07.22

Supervisor

Associate Professor,  
School of Biomedical Engineering,  
Indian Institute of Technology (BHU),  
Varanasi - 221005, (U.P.), India

SUPERVISOR


## DECLARATION BY THE CANDIDATE

I, **Neelima Varshney**, certify that the work embodied in this thesis is my own bona fide work and carried out by me under the supervision of **Dr. Sanjeev Kumar Mahto** from **January 2017 to July 2022** at the School of Biomedical Engineering, Indian Institute of Technology (Banaras Hindu University), Varanasi. The matter embodied in this thesis has not been submitted for the award of any other degree/diploma.

I declare that I have faithfully acknowledged and given credits to the research workers wherever their works have been cited in my work in this thesis. I further declare that I have not wilfully copied any other's work, paragraphs, text, data, results, *etc.*, reported in journals, books, magazines, reports dissertations, theses, *etc.*, or available at websites and have not included them in this thesis and have not cited as my own work.

**Date:** 18.07.2022

**Place:** Varanasi


  
**Signature of the Student**  
(Neelima Varshney)

## CERTIFICATE BY THE SUPERVISOR

It is certified that the above statement made by the student is correct to the best of our knowledge.

  
(Dr. Sanjeev Kumar Mahto)  
**Supervisor**  
Associate Professor  
School of Biomedical Engineering,  
Indian Institute of Technology  
(Banaras Hindu University)  
Varanasi – 221005, (U.P.), India

**SUPERVISOR**

  
(Dr. Sanjeev Kumar Mahto)  
**Coordinator**  
Associate Professor  
School of Biomedical Engineering,  
Indian Institute of Technology  
(Banaras Hindu University)  
Varanasi – 221005, (U.P.), India

समन्वयक/CO-ORDINATOR  
जैव चिकित्सा अभियांत्रिकी स्कूल  
SCHOOL OF BIOMEDICAL ENGG.  
भारतीय प्रौद्योगिकी संस्थान (का.हि.वि.)  
INDIAN INSTITUTE OF TECHNOLOGY (B.H.U.)  
वाराणसी-221005/VARANASI-221005

## COPYRIGHT TRANSFER CERTIFICATE

**Title of the Thesis:** Fabrication and Characterization of Three-dimensional  
Functional Scaffolds for Skin Tissue Engineering.

**Name of the Student:** Neelima Varshney

### Copyright Transfer

The undersigned hereby assigns to the Indian Institute of Technology (Banaras Hindu University), Varanasi all rights under copyright that may exist in and for the above thesis submitted for the award of the Doctor of Philosophy.

**Date:** 18.07.2022

**Place:** Varanasi

  
(Neelima Varshney)

**Note:** However, the author may reproduce or authorize others to reproduce material extracted verbatim from the thesis or derivative of the thesis for author's personal use provided that the source and the Institute's copyright notice are indicated.

## ACKNOWLEDGEMENTS

---

It is my greatest pleasure to have this opportunity to express my sincere appreciation to everyone who helped me during my Ph.D. program at the Indian Institute of Technology (Banaras Hindu University), Varanasi. First and foremost, I want to express my deepest gratitude to the almighty for giving this wonderful life and everything. Then, I want to thank my supervisor **Dr. Sanjeev Kumar Mahto**, for his valuable guidance, encouragement and his paternal behaviour throughout the work. His inspiring and excellent guidance is the key reason that I could successfully finish each of the research objectives. Without his guidance as a great mentor, this work would not have been possible.

I would like to express my gratitude to my research progress evaluation committee (RPEC) members, Dr. Manoj Kumar and Dr. Ashutosh Kumar Dubey, for their kind cooperation during the course of this work. I offer my special thanks to Dr. Sanjeev Kumar Mahto, Coordinator of the School of Biomedical Engineering for providing all the necessary facilities of the School.

I would like to thanks Prof. Rajeev Prakash, In-Charge, Central Instrument Facility Centre and his team members for providing all the characterization facilities on time with precision, without which the completion of this work was not possible. I also wish to express thankfulness to all other respected faculty members of the School for their kind support and valuable suggestions.

I would like to thank my wonderful lab-mates Dr. Kiran Y. Vajanthri, Dr. Suruchi Poddar, Dr. Niraj K. Vishwakarma, Dr. Ajay, Shravanya, Snehalata, Pooja, Parul, Richa, Sushmitha, Priya, Narayan, and Piyush for their stimulating discussions and creating a cheerful environment in the lab. I would also like to thank my batch-mates and friends Dr. Nitesh Malan, Mr. Rahul, Mr. Alok, Mr. Taresh, Mr. Chandrakant and Mr. Sagar and

all my juniors for their extended support. This thesis would not have been possible without the co-operation of my room-mate Ms. Sonam and among others Ms. Pragya, Ms. Anita, and Ms. Jyoti. I thank all my beloved friends across the globe for sharing my happy and sorrow moments at all times especially Mr. Saddam Hussain, Ms. Anshi Vishnoi and Ms. Vaishali. Sincere thanks to Mr. Kishori Ji for taking care of all non-academic aspects necessary for smooth working in the lab.

I would like to sincerely thank to all the supporting staff of the School for their kind help whenever I required.

I am extremely thankful to my family who has always been with me during all the ups and down of my Ph.D. journey. Without the support of my parents, in-laws, and my best friend my husband, I would not have made this far. I can never forget my parents, in-laws, brothers and sister whose boundless love, constant inspiration, emotional support and blessings has provided me encouragement at every step of life. My parents' everlasting shower of blessing kept me moving easily with all hazards vanishing miraculously. My word power fails to express my feeling of gratitude to my loving family members for their encouragement and moral support during my work.

**Date:** 18.07.2022

**Place:** Varanasi

  
(Neelima Varshney)

***Dedicated***  
***To***  
***My Beloved***  
***Parents and In-***  
***laws,***  
***My Dear Husband,***  
***My Loving***  
***Brothers and Sister***

<b>Table of Contents</b>	<b>Page No.</b>
<b>LIST OF FIGURES .....</b>	<b>xiii</b>
<b>LIST OF TABLES .....</b>	<b>xxix</b>
<b>LIST OF ABBREVIATIONS AND SYMBOLS .....</b>	<b>xxxii</b>
<b>PREFACE .....</b>	<b>xxxv</b>
<b>Chapter 1.....</b>	<b>1</b>
<b>Introduction .....</b>	<b>1</b>
<b>1.1 Tissue engineering .....</b>	<b>2</b>
<b>1.1.1 Extracellular matrix .....</b>	<b>3</b>
<b>1.1.2 Advantages of three-dimensional (3D) cell culture.....</b>	<b>5</b>
<b>1.1.3 Scaffolds and their fabrication techniques.....</b>	<b>8</b>
<b>1.1.4 Scaffold-based tissue engineering approaches.....</b>	<b>15</b>
<b>1.2 Skin tissue.....</b>	<b>17</b>
<b>1.2.1 Skin tissue anatomy .....</b>	<b>17</b>
<b>1.2.2 Functions .....</b>	<b>18</b>
<b>1.2.3 Wound healing.....</b>	<b>18</b>
<b>1.2.4 Wound dressing.....</b>	<b>21</b>
<b>1.3 Review of the existing literature .....</b>	<b>24</b>
<b>1.4 Research objectives .....</b>	<b>29</b>
<b>1.5 Thesis outline .....</b>	<b>31</b>
<b>1.6 References .....</b>	<b>36</b>
<b>Chapter 2.....</b>	<b>45</b>
<b>Fabrication and Characterization of Silk Fibroin- Soy Protein based Nanofibrous Scaffolds for Skin Tissue Engineering.....</b>	<b>45</b>
<b>2.1 Introduction .....</b>	<b>46</b>
<b>2.2 Materials and methods.....</b>	<b>49</b>
<b>2.2.1 Materials .....</b>	<b>49</b>
<b>2.2.2 Preparation of dry silk fibroin film .....</b>	<b>50</b>
<b>2.2.3 Preparation of protein blend solution for electrospinning.....</b>	<b>51</b>
<b>2.2.4 Characterization of the scaffolds .....</b>	<b>53</b>

2.2.5 Statistical analysis .....	59
<b>2.3 Results .....</b>	<b>60</b>
2.3.1 SEM analysis of the fabricated electrospun mats .....	60
2.3.2 ATR-FTIR spectroscopic analysis of electrospun mats .....	65
2.3.3 Raman spectroscopy analysis .....	68
2.3.4 Swelling capacity.....	69
2.3.5 Stability and degradation of electrospun nanofibers.....	70
2.3.6 Transparency percentage of the fabricated nanofibrous scaffolds .....	72
2.3.7 Thermal stability of the fabricated nanofibrous sheets.....	73
2.3.8 Cytocompatibility of the fabricated nanofibrous scaffolds.....	74
2.3.9 In vivo wound healing.....	79
<b>2.4 Discussion .....</b>	<b>80</b>
<b>2.5 Summary.....</b>	<b>86</b>
<b>2.6 References.....</b>	<b>88</b>
<b>Chapter 3 .....</b>	<b>99</b>
<b>Fabrication and Characterization of Polyvinyl Alcohol- Soy Protein Composite Hydrogels for Skin Tissue Engineering .....</b>	<b>99</b>
<b>3.1 Introduction.....</b>	<b>100</b>
<b>3.2 Materials and methods .....</b>	<b>103</b>
3.2.1 Materials .....	103
3.2.2 Synthesis of hydrogels .....	103
3.2.3 Characterization of the hydrogels .....	105
<b>3.3 Results .....</b>	<b>113</b>
3.3.1 Gel fraction.....	113
3.3.2 Porosity .....	115
3.3.3 Surface wettability .....	116
3.3.4 SEM analysis of the fabricated FT hydrogels .....	117
3.3.5 Swelling capacity.....	119

3.3.6 Water vapor transmission rate .....	120
3.3.7 Stability and degradation of FT hydrogels .....	121
3.3.8 ATR-FTIR spectroscopic analysis of FT hydrogels .....	124
3.3.9 X-ray diffraction (XRD) analysis.....	125
3.3.10 Differential scanning calorimetry analysis .....	126
3.3.11 Thermal stability of FT hydrogels .....	127
3.3.12 Mechanical properties of FT hydrogels .....	129
3.3.13 Cellular biocompatibility of FT hydrogels.....	132
3.3.14 In vivo wound healing.....	136
3.4 Discussion .....	138
3.5. Summary .....	143
3.6 References .....	145
<b>Chapter 4.....</b>	<b>153</b>
<b>Preparation and Characterization of Highly Porous Soy protein Cryogel for Skin Tissue Engineering.....</b>	<b>153</b>
4.1 Introduction .....	154
4.2 Materials and methods.....	156
4.2.1 Materials .....	156
4.2.2 Synthesis of cryogels.....	157
4.2.3 Characterization of the cryogels .....	158
4.3 Results .....	167
4.3.1 Morphological analysis of the prepared SPI cryogels.....	167
4.3.2 Porosity of SPI cryogels .....	170
4.3.3 Swelling ability and water retention capacity of the prepared SPI cryogels.....	171
4.3.4 Stability and degradation of SPI cryogels.....	175
4.3.5 FTIR analysis.....	176
4.3.6 Thermal properties of prepared SPI cryogels .....	177

4.3.7 Mechanical properties .....	179
4.3.8 Hemocompatibility of SPI cryogels .....	184
4.3.9 In vitro blood clotting performance of SPI cryogels .....	185
4.3.10 Cellular biocompatibility of prepared SPI cryogels .....	187
4.3.11 In vivo wound healing.....	190
4.4 Discussion .....	192
4.5 Summary.....	199
4.6 References .....	201
<b>Chapter 5 .....</b>	<b>209</b>
<b>Fabrication and Characterization of Macroporous PDMS based Scaffold for Tissue Engineering.....</b>	<b>209</b>
5.1 Introduction.....	210
5.2 Materials and methods .....	212
5.2.1 Materials .....	212
5.2.2 Fabrication of macroporous PDMS scaffold.....	213
5.2.3 Characterization of macroporous PDMS Scaffolds .....	214
5.3 Results .....	221
5.3.1 Morphological characterization of the porous networks of PDMS scaffolds.....	221
5.3.2 Interconnectivity of the macroporous scaffold .....	222
5.3.3 Porosity of scaffold.....	224
5.3.4 Surface modification and wettability of scaffolds.....	225
5.3.5 Liquid retainability of the scaffold.....	226
5.3.6 Mechanical property of PDMS based scaffolds .....	227
5.3.7 Co-culture and cellular proliferation within PDMS scaffolds.....	228
5.4 Discussion .....	232
5.5. Summary.....	238
5.6 References .....	240

<b>Chapter 6.....</b>	<b>247</b>
<b>Conclusions and Future Scope of Work.....</b>	<b>247</b>
<b>Permission from Central Animal Ethical Committee.....</b>	<b>253</b>
<b>Permission from Istitutional Ethics Committee .....</b>	<b>254</b>
<b>List of Publications.....</b>	<b>255</b>

## **LIST OF FIGURES**

---

<b>Figure No.</b>	<b>Figure description</b>	<b>Page No.</b>
<b>Figure 1.1</b>	Tissue engineering triad: scaffold, signals and cells.	3
<b>Figure 1.2</b>	Structural components of ECM and its various functions.	4
<b>Figure 1.3</b>	Schematic representation showing the comparison between 2D and 3D cell culture environment.	8
<b>Figure 1.4</b>	Desired properties of tissue engineering scaffolds.	9
<b>Figure 1.5</b>	Various porous scaffold fabrication techniques: (A) Porogen leaching (B) Gas foaming (C) Freeze-thawing (D) Solution electrospinning (E) Soft lithography (3D printing).	15
<b>Figure 1.6</b>	Schematic representation of various scaffolding tissue engineering approaches: acellular and cellular constructs.	17
<b>Figure 1.7</b>	Skin anatomy: skin consist of three main layers, namely- 1) epidermis 2) dermis and 3) hypodermis or subcutaneous layer.	18
<b>Figure 1.8</b>	Wound healing phases and the function of biopolymers at each stage.	20
<b>Figure 1.9</b>	Wounds classification on the basis of wound depth.	20
<b>Figure 1.10</b>	Advantages of moist wound environment over the dry wound environment.	22
<b>Figure 1.11</b>	Classification of skin substitutes on the basis of replaced region, cellularity, permanency, material utilized and layering. (b) Some examples of commonly used biomaterials in tissue engineering.	24

<b>Figure 1.12</b>	Schematic representation of Chapter 2 (Fabrication and Characterization of SF- Soy protein based Nanofibrous Scaffolds for Skin Tissue Engineering).	32
<b>Figure 1.13</b>	Schematic representation of Chapter 3 (Fabrication and Characterization of PVA- Soy Protein Composite Hydrogels for Skin Tissue Engineering).	33
<b>Figure 1.14</b>	Schematic representation of Chapter 4 (Preparation and Characterization of Highly Porous Soy Protein Cryogels for Skin Tissue Engineering).	34
<b>Figure 1.15</b>	Schematic representation of Chapter 5 (Fabrication and Characterization of Macroporous PDMS based Scaffolds for Tissue Engineering).	35
<b>Figure 2.1</b>	Schematic representation of procedure of silk fibroin (SF) extraction from Bombyx mori silk Cocoons.	51
<b>Figure 2.2</b>	Schematic representation of SPI/SF electrospun mat fabrication process using electrospinning technique.	53
<b>Figure 2.3</b>	Morphological analysis through SEM photomicrograph of electrospun sheet of 100 SPI solution at different magnifications.	61
<b>Figure 2.4</b>	Morphological analysis through SEM photomicrographs of the prepared nanofibrous scaffolds with different SPI/SF blend compositions, namely: 100 SF, 75/25 SPI/SF, 50/50 SPI/SF, and 25/75 SPI/SF along with their respective fiber orientation graphs. Scale bar: 1 $\mu$ m.	62
<b>Figure 2.5</b>	Diameter distribution of nanofibers for different compositions of nanofibrous electrospun scaffolds: 100 SF (NT), 100 SF (T),	63

25/75 SPI/SF (NT), 25/75 SPI/SF (T), 50/50 SPI/SF (NT), 50/50 SPI/SF (T), 75/25 SPI/SF (NT) and 75/25 SPI/SF (T).

- Figure 2.6** Graph depicting the porosity percentage of nanofibrous scaffolds analyzed by applying the threshold function on SEM micrographs. Values are expressed as mean  $\pm$  SD (n = 5) and the level of significance as \*\*\*p < 0.05. 65
- Figure 2.7** ATR-IR spectra of (a) SPI/SF (NT) (b) EtOH vapor treated SPI/SF (T) blend electrospun nanofibers. (c–g) Comparison between ATR-IR spectra of EtOH vapor treated and non-treated various SPI/SF blend electrospun nanofibers: 100 SPI, 100 SF, 25/75 SPI/SF, 50/50 SPI/SF and 75/25 SPI/SF. 67
- Figure 2.8** Raman spectra of electrospun SPI/SF nanofibers: (a) ethanol vapor treated (T) and non-treated (NT) nanofibers (A) 100 SF (NT) (B) 100 SF (T) and (b) ethanol treated (T) all the fabricated nanofibers (A) 100 SF (B) 25/75 SPI/SF (C) 50/50 SPI/SF. 68
- Figure 2.9** Graph shows weight gain percentage of different nanofibrous scaffolds of various ratios of SF and SPI, before and after ethanol vapor treatment in PBS at a room temperature (25 °C) (a) 100 SF (b) 25/75 SPI/SF (c) 50/50 SPI/SF electrospun scaffold (d) comparison of weight gain percentage of nanofibrous scaffolds. Values are expressed as mean  $\pm$  SD (n = 3) and the level of significance as \*\*\*p < 0.05. 70
- Figure 2.10** Represents (a) digital images depicting stability of prepared nanofibrous scaffolds in PBS at a room temperature (b) digital images of scaffolds held through forceps after 10 day immersion 72

in PBS at 37 °C, (c) and (d) digital and SEM micrographs of electrospun samples, respectively, after 20 days degradation in lysozyme containing solution at 37 °C (e) graph shows weight loss percentage of samples over 20 days of immersion in lysozyme-containing solution at 37 °C. Values are expressed as mean  $\pm$  SD (n = 3) and the level of significance as \*\*\*p < 0.05. Scale bar is 800 nm for SEM images.

- Figure 2.11** Transparency of different nanofibrous scaffolds of various ratios of SF and SPI before (NT) and after ethanol vapor treatment (T) in PBS at a room temperature (25 °C) (a) digital images of samples showing visual transparency (b) graph shows percentage of light transmission through the samples. Scale bar: 4 mm. Values are expressed as mean  $\pm$  SD (n = 3). 73
- Figure 2.12** TGA curve of EtOH vapor treated (T) and non-treated (NT) various SPI/SF blend electrospun nanofibers: (a) 100 SF (b) 25/75 SPI/SF (c) 50/50 SPI/SF, (d) non-treated samples (e) treated samples. 74
- Figure 2.13** The above panel of images represents the culture of L929-RFP (fibroblast) Left: 50/50 SPI/SF, middle: 25/75 SPI/SF and right: 100 SF for over a period of 7 days. Scale bar is 100  $\mu$ m for brightfield, fluorescent and merged images. 75
- Figure 2.14** The above panel of images represents the culture of B16-F10 (melanocytes) cells within the nanofibrous scaffolds. Left: 50/50 SPI/SF, middle: 25/75 SPI/SF and right: 100 SF for over a period 76

of 7 days. Scale bar is 100  $\mu\text{m}$  for brightfield, fluorescent and merged images.

- Figure 2.15** The figure illustrates the percentage cellular viability of (a) NIH-3T3 cells and (b) B16-F10 cells for 2 and 4 days and the compatibility of the nanofibrous scaffolds determined by MTT assay (c) comparative cellular viability percentage of NIH-3T3 cells and B16-F10 cells within nanofibrous scaffolds with respect to ratio of soy protein isolate (SPI). In MTT assay experiment, absorbance for the 4th day culture of positive control was taken as reference OD for all the samples. Values are expressed as mean  $\pm$  SD (n = 3) and the level of significance as \*\*\*p < 0.05. 78
- Figure 2.16** The figure illustrates SEM images of NIH-3T3 (fibroblast) cells cultured on fabricated nanofibrous scaffolds. Scale bar is 20  $\mu\text{m}$  for SEM images. 79
- Figure 2.17** Shows in vivo wound healing (a) digital photographs of full thickness wound closure on day 1, 3, 8, 11 and 14 (b) graph depicts a comparison of wound area closed percentage of treated and sham (untreated) groups (c) and (d) H&E staining image of the histological section of 50/50 SPI/SF (T) and sham, respectively, after 14 days. Values are expressed as mean  $\pm$  SD (n = 3) and the level of significance as \*\*\*p < 0.05. Scale bar: 100  $\mu\text{m}$ . 80
- Figure 3.1** Schematic representation of fabrication process of freeze-thawed PVA/SPI scaffolds. 105

<b>Figure 3.2</b>	Digital images fabricated all FT PVA/SPI hydrogels: before FT, after FT and after lyophilisation.	105
<b>Figure 3.3</b>	(a) Digital images of all the fabricated FT PVA/SPI hydrogels. (b) Graph depicting gel fraction percentage. Values are expressed as mean $\pm$ SD (n = 5).	114
<b>Figure 3.4</b>	Graph depicting porosity percentage of PVA/SPI composite FT scaffolds. Values are expressed as mean $\pm$ SD (n = 5) and the level of significance as ***p < 0.05.	116
<b>Figure 3.5</b>	Graph depicting surface wettability of all the fabricated FT hydrogels. Values are expressed as mean $\pm$ SD (n = 5) and the level of significance as ***p < 0.05.	117
<b>Figure 3.6</b>	Morphological analysis through SEM photomicrographs (different magnifications) of all the prepared FT hydrogel samples with different PVA/SPI composite compositions, namely, 100% PVA, 90/10 PVA/SPI, 70/30 PVA/SPI, 50/50 PVA/SPI, and 100% SPI, along with their respective pore size distribution graphs.	118
<b>Figure 3.7</b>	Graphs showing (a) weight gain percentage (b) maximum water content percentage of all the prepared freeze–thawed hydrogel samples, namely, 100% PVA, 90/10 PVA/SPI, 70/30 PVA/SPI, and 50/50 PVA/SPI, in PBS at room temperature (25 °C). (c) Digital images of all samples after 12 h of swelling in PBS. Values are expressed as mean $\pm$ SD (n = 5). Scale bar: 10 mm.	120
<b>Figure 3.8</b>	(a) Graph showing the water vapor transfer rate (WVTR). (b) Digital images showing freeze–thawed samples (100% PVA,	121

90/10 PVA/SPI, 70/30 PVA/SPI, and 50/50 PVA/SPI) in PBS solution after 7 and 14 days of in vitro degradation. (c, d) Graphs showing weight loss percentage of all the prepared FT hydrogel samples in lysozyme-containing solution and PBS solution, respectively, at 37 °C. Values are expressed as mean  $\pm$  SD (n = 3) and the level of significance as \*\*\*p < 0.05.

- Figure 3.9** SEM micrographs along with their respective pore size distribution graphs of FT samples after 14 days of in vitro degradation in lysozyme-containing solution at 37 °C. Values are expressed as mean  $\pm$  SD (n = 5) and the level of significance as \*\*\*p < 0.05. 123
- Figure 3.10** Chemical structure analysis: (a) FTIR spectra of (A) 100% SPI, (B) 50/50 PVA/SPI, (C) 70/30 PVA/SPI, (D) 90/10 PVA/SPI, (E) 100% PVA, and (b) 100% SPI FT hydrogel and SPI powder. (c) Schematic diagram representing the interaction (hydrogen bond formation) between PVA–PVA and PVA–SPI chains. 125
- Figure 3.11** X-ray diffraction profiles of all the fabricated PVA/SPI FT hydrogels. 126
- Figure 3.12** DSC curves of all the fabricated PVA/SPI FT hydrogels. 127
- Figure 3.13** TGA graph of all the fabricated PVA/SPI FT hydrogels. 129
- Figure 3.14** (a) Digital images of all the fabricated FT 70/30 PVA/SPI hydrogel (wet condition). (b) Compressive stress-strain curves at 50% strain under loading and unloading cycle (c) Digital images of all the fabricated freeze-thawed PVA/SPI hydrogels in compressed state and in relaxed state after pressure released. 130

Graph shows the (d) compressive strength and (e) compressive modulus values of all the fabricated PVA/SPI freeze-thawed hydrogels. Values are expressed as mean  $\pm$  SD (n = 3) and the level of significance as \*\*\*p < 0.05.

- Figure 3.15** Correlation plots of compressive modulus versus gel fraction (%) , porosity (%), swelling (%) and pore sizes for the PVA/SPI FT hydrogels. 131
- Figure 3.16** The above panel of microscopic images represents the culture of L929-RFP (fibroblast) cells within the FT scaffolds for over a period of 12 days. Scaffolds without cells were taken as control. The scale bar is 100  $\mu$ m for bright-field, fluorescence, and merged images. 133
- Figure 3.17** Z stacking of the images: L929-RFP cells distribution within the PVA/SPI FT scaffolds. 134
- Figure 3.18** SEM images of L929-RFP (fibroblast) cells cultured on fabricated freeze-thawed scaffolds: (a) 100% PVA, (b) 90/10 PVA/SPI, (c) 70/30 PVA/SPI, and (d) 50/50 PVA/SPI. Scale bar: 20  $\mu$ m. 135
- Figure 3.19** Percentage cellular viability of NIH-3T3 (fibroblast) cells and the compatibility of the scaffolds determined by the MTT assay. In the MTT assay experiment, the absorbance for the 4<sup>th</sup> day culture of positive control was taken as the reference OD for all the samples. Values are expressed as mean  $\pm$  SD (n = 3) and the level of significance as \*\*\*p < 0.05. 136

- Figure 3.20** Figure showing in vivo wound healing: (a) digital photographs of full thickness wound closure on days 0, 2, 5, 8, 11, 13, and 15. (b) H&E staining image of the histological section of (i) sham, (ii) 90/10 PVA/SPI, (iii) 70/30 PVA/SPI, and (iv) 50/50 PVA/SPI after 15 days. (c) Graph depicting a comparison of wound area closed percentage of treated and sham (untreated) groups. Values are expressed as mean  $\pm$  SD ( $n = 3$ ) and the level of significance as \*\*\* $p < 0.05$ . Scale bar: 50  $\mu\text{m}$ . 137
- Figure 4.1** Schematic representation of the fabrication process of GA cross-linked superporous SPI scaffolds using cryogelation technique. 158
- Figure 4.2** Digital images of (a) all the prepared SPI cryogels after thawing and their respective disc shaped section showing transparency property of the samples and (b) light-weight prepared cylindrical SPI cryogel (lyophilized) supported by a palm leaf tip, respectively. 169
- Figure 4.3** Morphological analysis through SEM photomicrographs at different magnifications of all the prepared lyophilised SPI cryogel samples of different concentrations: 10%, 8%, 6%, 4% and 2% SPI, along with their respective pore size distribution graphs. 170
- Figure 4.4** Porosity percentage of all the prepared SPI cryogel scaffolds. Values are expressed as mean  $\pm$  SD ( $n = 3$ ) and the level of significance as \*\*\* $p < 0.05$ . 171
- Figure 4.5** Graphs showing (a) weight gain percentage up to 48 h (b) maximum water content percentage of all the prepared 172

lyophilised SPI cryogel samples of different concentrations: 10%, 8%, 6%, 4% and 2% SPI, in PBS at room temperature (25 °C). (c) Digital images of all samples: dry state (before swelling), wet state (after 1 h and 48 h of swelling in PBS). Values are expressed as mean  $\pm$  SD (n = 5). Scale bar: 10 mm.

- Figure 4.6** Swelling (%) versus pore sizes and porosity (%) plots for the fabricated SPI cryogels. 173
- Figure 4.7** Digital images show cyclic swelling (swelling and squeezing) of SPI cryogels by performing manual compression. 174
- Figure 4.8** Changes of water retention rate with respect to time at 37 °C and 50% relative humidity. 175
- Figure 4.9** Degradation study: (a) digital images showing SPI cryogel samples (10%, 8%, 6%, 4% and 2% SPI) in PBS solution before and after 12 days of in vitro degradation. (b) SEM micrographs of lyophilized SPI cryogel samples after 12 days of in vitro degradation in PBS solution at 37 °C. Scale bar: 100  $\mu$ m. (c, d) graphs showing weight loss percentage of all the prepared SPI cryogel samples in PBS and lysozyme-containing solution, respectively, at 37 °C. Values are expressed as mean  $\pm$  SD (n = 3) and the level of significance as \*\*\*p < 0.05. 176
- Figure 4.10** FTIR spectra of all the prepared SPI cryogel scaffolds. 177
- Figure 4.11** (a) TGA (b) DTA curves and (c) DSC curves of SPI powder, 4%, 6% and 8% SPI cryogels. 178
- Figure 4.12** Mechanical properties of prepared SPI cryogels: (a) photographs of the compression behaviour of 6% SPI cryogel under 180

instrumental control. Cycle curves were obtained immediately after one loading-unloading cycle of SPI cryogels at (b) 50% compression (c) 80% compression. (d) Compressive modulus values of 4%, 2% and 8% SPI cryogels.

- Figure 4.13** Compressive stress-strain curves at 50% strain under 10 loading-unloading cycles of (a) 4% SPI, (b) 6% SPI and (c) 8% SPI cryogel samples. Compressive stress-strain curves at 80% strain under 10 loading-unloading cycles of (d) 4% SPI, (e) 6% SPI and (f) 8% SPI cryogel samples. 181
- Figure 4.14** Shape recovery properties of the cryogel: original state in a wet condition, before compression, compressed state (fixed shape) after releasing all free water, after compression recovered shape by reabsorbing the released water. 183
- Figure 4.15** (a) Images from haemolytic activity assay of the SPI cryogels using PBS as negative control (N.C.) and distilled water as positive control (P.C.). (b) Haemolytic percentage of the SPI cryogels' dispersion liquids. In vitro hemostatic capacity evaluation of SPI cryogels (c) in vitro whole blood clotting evaluation of cryogels and controls (gauze and cotton). 185
- Figure 4.16** SEM images of blood cells adhesion on the SPI cryogels and controls (gauze and cotton). Scale bar: 100  $\mu\text{m}$  for 400X; 10  $\mu\text{m}$  for 2000X; 2  $\mu\text{m}$  for 10000X. 187
- Figure 4.17** The above panel of microscopic images represents the culture of L929 (fibroblast) cells within the SPI cryogels for over a period of 10 days. Cryogels without cells were taken as control. Scale 188

bar: 100  $\mu\text{m}$  for bright-field, fluorescence, and merged images. The fluorescence images in the dotted rectangle are at different magnifications to clearly visualize the nucleus (DAPI staining) of the cultured cells within the SPI cryogels.

**Figure 4.18** SEM images of L929 (fibroblast) cells cultured on SPI cryogels: 4%, 6% and 8% SPI cryogels. Scale bar: 100  $\mu\text{m}$ . 189

**Figure 4.19** Percentage cellular viability of L929 (fibroblast) cells and the compatibility of the SPI cryogels determined by the MTT assay. In the MTT assay experiment, the absorbance for the 7<sup>th</sup> day culture of positive control (cultured cells without cryogel samples) was taken as the reference OD for all the samples. Values are expressed as mean  $\pm$  SD (n = 3) and the level of significance as \*\*\*p < 0.05. 190

**Figure 4.20** Figure showing in vivo wound healing: (a) digital photographs of full thickness excision wound and application of SPI cryogel to the wound (b) digital photographs of full thickness wound closure on days 0, 4, 10, 14, and 16. (c) Graph depicting a comparison of wound area closed percentage of cryogel treated and sham (untreated) groups (d) micrographs of H&E stained tissues: (i) sham group, (ii) 4% SPI treated, (iii) 6% SPI treated skin tissues; higher magnifications images of histological sections (H&E stains) of 6% SPI treated skin tissues in dotted rectangle. In cryogel treated wounds, the connective tissue is found to be more organized and developed than the untreated 192

wounds. Values are expressed as mean  $\pm$  SD (n = 3) and the level of significance as \*\*\*p < 0.05. Scale bar: 50  $\mu$ m.

- Figure 5.1** Schematic representation of porous PDMS scaffold fabrication process using salt leaching method. 213
- Figure 5.2** SEM micrograph of PDMS scaffolds with the corresponding EDX spectra and element analysis (a) before leaching and (b) after leaching of 2:1 PDMS scaffold, (c) after leaching of 3:1 PDMS scaffold and (d) quantitative analysis of SEM micrographs using Image J software represent wide distribution of pore size across the scaffolds. Quantitative data were calculated using at least 5 images captured from the three independent experiments. 222
- Figure 5.3** Representative micrographs reveal interconnectivity of the pores within the PDMS scaffolds (a) (i) plasma treated (PT) scaffolds (2:1 and 3:1 PDMS scaffold, 10 mm diameter x 3.7 mm height) imbibed with water (for t = 10 min), (ii) a food coloring dye placed on top of the water-soaked PT scaffolds, (iii) dye seepage from top to the entire volumetric space of the scaffold, (iv) cross-section of the scaffold confirming transport of the dye through the interconnected pores, (b) transport of the dye over time across the scaffold from a dye filled reservoir to an empty reservoir which were set 40 mm apart from each other [captured in real time using a digital camera with a video mode (30 fps)], (c) diffusion profile of the dye that was calculated through intensity profile across the scaffolds using an Image J software. 223

The images were captured using a digital camera (1920 x 1080, 16.1 megapixels). Scale bar: 2.5 mm

- Figure 5.4** Graphs represent (a) the retained volume and (b) porosity percentage within the scaffold. Data represent mean  $\pm$  standard deviation of three independent experiments. The statistical differences between the samples are represented by \* $p < 0.05$ ; \*\* $p < 0.01$ ; \*\*\* $p < 0.001$ . 225
- Figure 5.5** Surface water wettability of different types of the PDMS samples. (a) Digital images of a water droplet on different types of PDMS samples before and after plasma treatment (UT untreated, PT plasma treated) and (b) the contact angle values measured using Image J software. Data represent mean  $\pm$  standard deviation of three independent experiments. The statistical differences between the samples are represented by \* $p < 0.05$ ; \*\* $p < 0.01$ ; \*\*\* $p < 0.001$ . 226
- Figure 5.6** Graphs represent percentage of liquid absorption in different types of PDMS scaffolds before and after plasma treatment: after 48 h and 1 h of soaking in water. Data are presented as mean  $\pm$  SD obtained through three independent experiments performed in triplicate. 227
- Figure 5.7** The stress–strain plot in compression for solid PDMS, porous PDMS of 2:1 and 3:1 (w/w). Data in plot represent the values of three independent experiments ( $n = 3$ ). Obtained values are presented in table number 2. 228

**Figure 5.8** Representative images show cell culture within the PDMS based scaffolds (a) fluorescent intensity of L929 (fibroblast) RFP cells observed on the various days when cultured within the PDMS scaffolds. (b) Rhodamine-phalloidin (F-actin) and DAPI (nuclear) stained images of B16-F10 (melanocyte) cells cultured within the PDMS scaffolds for various days. Z stacking of the image reveals the cellular network of (c) L929 RFP within the 560  $\mu\text{m}$  thick scaffold and (d) co-culture of L929-RFP with B16-F10 cells using a laser confocal microscope within the 350  $\mu\text{m}$  thick scaffold. Scale bar: 100  $\mu\text{m}$ . 230

**Figure 5.9** Method for showing the nuclei of B16-F10 cells in co-culture with L929-RFP using ImageJ software. Upper panel: fluorescent images of DAPI stained nuclei of both the cells (left), L929-RFP cells (middle) and merged image of first two images (right); non-overlapping blue spots exhibit the nuclei of B16-F10 cells (white arrow) and the blue spots overlapped with red mark show the nuclei of L929-RFP cells (yellow arrow). Middle panel: transformed grayscale images of L929-RFP and merged images. Lower panel: grayscale images were converted into binary images at a suitable threshold value and then subtracted to represent the nuclei of B16-F10 cells only, in a new subtracted binary image. Binary images (right to left): merged, L929-RFP and an image obtained after subtraction of L929-RFP binary 231

image from a merged binary image that helps in the visualization of B16-F10 nuclei separately. Scale bar: 100  $\mu\text{m}$

**Figure 5.10** The representative graph shows cell proliferation within the PDMS based scaffold using the MTT assay (a) L929 fibroblast cells and (b) B16-F10 melanocyte cells cultured within the fabricated scaffolds with different salt to pre-polymer PDMS ratios (w/w) after 2, 5 and 7 days of culture. Cells cultured in wells (i.e., without scaffold) were considered as a control. The percentage of cell proliferation was calculated by the ratio of absorbance of test sample to the absorbance of control (at 7 days). Experiments were performed in triplicates for both cell types along with their respective controls. Data represent mean  $\pm$  standard deviation of three independent experiments. The statistical differences between the same type of scaffold at different time of culture are represented by \* $p < 0.05$ ; \*\* $p < 0.01$ ; \*\*\* $p < 0.001$ .

## **LIST OF TABLES**

---

<b>Table No.</b>	<b>Table description</b>	<b>Page No.</b>
<b>Table 1.1</b>	Analogous functions of ECM and TE scaffolds.	7
<b>Table 2.1</b>	Formulations of spinning solutions containing SPI and SF in formic acid.	52
<b>Table 2.2</b>	Optimized values of electrospinning parameters for the prepared formulations.	52
<b>Table 2.3</b>	Morphology, mean diameter and porosity of electrospun nanofibrous mats with various compositions.	64
<b>Table 3.1</b>	Formulations of freeze-thawed PVA/SPI composite hydrogels.	104
<b>Table 3.2</b>	Various parameters of PVA/SPI freeze-thawed hydrogels with various compositions.	115
<b>Table 3.3</b>	Thermal properties of freeze-thawed PVA/SPI hydrogels based on DSC and TGA thermograms.	128
<b>Table 3.4</b>	Correlation values between variables.	130
<b>Table 4.1</b>	Formulations of various fabricated SPI cryogels.	158
<b>Table 4.2</b>	Mechanical properties of prepared SPI cryogels: Compressive strength at 50% and 80% compression, and compressive modulus.	180
<b>Table 4.3</b>	Shape fixity ratio, recovery ratio and volumetric expansion ratio of the water-triggered shape recovery process of the SPI cryogels.	183
<b>Table 5.1</b>	Apparent porosity, effective porosity and volume retained for solid PDMS, porous PDMS (2:1) and porous PDMS (3:1).	224



## **LIST OF ABBREVIATIONS AND SYMBOLS**

ECM	Extracellular matrix
TE	Tissue engineering
WHO	World Health Organization
2D	Two-dimensional
3D	Three-dimensional
PDMS	Polydimethylsiloxane
PVA	Poly (vinyl alcohol)
PLA	Poly-lactic acid
PCL	Polycaprolactone
PGA	Poly-glycolic acid
PLLA	Poly(L-lactic acid)
PLGA	Poly(lactic-co-glycolic acid)
PAN	Polyacrylonitrile
PEO	Polyethylene oxide
CAR	Carrageenan
SPNF	SPI-functionalized nanofibers
PTAC	Polyvinyl alcohol-tetraethylorthosilicate-alginate-calcium oxide
AM	Additive manufacturing
CAD	Computer aided design
MRI	Magnetic resonance imaging
CTs	Computed tomography scan

BM	Basement membrane
KC	Keratinocytes
TEWL	Transepidermal water loss
ROS	Reactive oxygen species
RGD	Arginine-Glycine-Aspartate
PEG	Poly (ethylene glycol)
EtOH	Ethanol
LiBr	Lithium bromide
SEM	Scanning electron microscopy
XRD	X-ray diffraction
TGA	Thermogravimetric analysis
DSC	Differential scanning calorimetry
MTT	(3-(4,5-Dimethylthiazol-2-yl)-2,5-Diphenyltetrazolium Bromide)
DMSO	Dimethyl Sulfoxide
ANOVA	Analysis of variance
MWC	Maximum water content
H&E	Haematoxylin and eosin
DMEM	Dulbecco's modified Eagle's medium
FBS	Fetal Bovine Serum
PBS	Phosphate buffer saline
SPI	Soy protein isolate
SF	Silk fibroin
T	Ethanol vapour treated
NT	Ethanol vapour non-treated

DAPI	(4,6-diamidino-2-phenylindole)
DNA	Deoxyribonucleic acid
ATR	Attenuated total reflection
FTIR	Fourier transform infrared
TEBM	Tissue Engineering and Biomicrofluidics
BSA	Bovine serum albumin
WVTR	Water vapour transmission rate
FT	Freeze-thawed
GF	Gel fraction
PT	Plasma-treated
GA	Glutaraldehyde
SD	Standard deviation
CA	Contact angle
Na <sub>2</sub> CO <sub>3</sub>	Sodium bicarbonate
kPa	Kilo Pascal
MPa	Mega Pascal
%	Percentage
mm	Millimetre
cm	Centimetre
nm	Nanometre
mM	Milli molar
μM	Micro molar
CO <sub>2</sub>	Carbon dioxide
rpm	Rotations per minute

t	Time
°C	Degree Celsius
g	Gram
U	Unit
h	hour
s	second
kV	Kilovolt
mL	Millilitre
μL	Microliter

## **PREFACE**

---

Burns, persistent wounds, and severe accidents may cause extensive skin loss, resulting in lifelong impairment of skin functions. The gold standard treatment approach for full-thickness wounds at present is a skin graft or split-thickness autologous skin transplant. However, many patients lack sufficient intact skin for such a treatment, and scar development renders this a cosmetically ineffective choice. Because of this, there is a demand for a tissue-engineered construct that promotes healing, prevents infection, and has a long shelf life.

The enabling scaffold fabrication methods for tissue engineering provide new opportunities to imitate the natural milieu of a cell sufficiently well to assist in the overall functions of a specific cell or tissue. In this thesis, we used electrospinning, freeze-thawing/cryogelation, and salt-leaching to make a variety of functional structures on the micro and nano scales.

The first part of the thesis presents the development of biocompatible soy protein isolate/silk fibroin (SPI/SF) nanofibrous scaffolds through electrospinning a novel protein blend SPI/SF. Prepared nanofibers were treated with ethanol vapor to obtain an improved water-stable structure. Fabricated scaffolds were characterized through scanning electron microscopy (SEM), Fourier transform infrared spectroscopy (FTIR), thermogravimetric analysis (TGA), UV–VIS spectrophotometry and image analysis. The scaffolds were found significantly stable for a prolonged duration at the room temperature as well as at 37 °C, when placed in phosphate buffered saline (PBS), nutrient medium, and lysozyme-containing solution. The potential of fabricated scaffolds for skin tissue regeneration was evaluated by *in vitro* culturing of standard cell lines *i.e.*, fibroblast cells (L929-RFP (red fluorescent protein) and NIH-3T3) and melanocytes (B16F10). The outcomes revealed

that all the fabricated nanofibrous scaffolds were non-toxic towards normal mammalian cells. In addition, healing of full-thickness wound in rats within 14 days after treatment with a nanofibrous scaffold demonstrated its suitability as a potential wound dressing material. Interestingly, we found that nanofibers induced a noticeable reduction in the proliferation rate of B16F10 melanoma cells.

In the second part of the thesis, we demonstrate the development of polyvinyl alcohol (PVA) and SPI based scaffolds by physical crosslinking using the freeze-thaw method. PVA/SPI ratio was varied to examine the individual effects of the two constituents. The physicochemical properties of the fabricated scaffolds were analyzed through FTIR, SEM, X-ray diffraction (XRD), TGA and differential scanning calorimetry (DSC). SPI concentration significantly affected the properties of scaffolds, such as the extent of gelation (%), pore size, porosity, degradation, swelling and surface wettability. The in vitro degradation of fabricated hydrogels was evaluated in PBS and lysozyme solution for a duration of fourteen days. The in vitro compatibility of prepared hydrogels was evaluated by MTT assay with NIH-3T3 cells (fibroblast). The water vapor transmission rate (WVTR) assays showed that all hydrogels possessed WVTR values in the range of 2000 to 2500 g m<sup>-2</sup>day<sup>-1</sup>, which is generally recommended for ideal wound dressing. Overall, the obtained results reveal that the fabricated scaffolds have excellent biocompatibility, mechanical strength, porosity, stability and degradation rate, and thus carry enormous potential for tissue engineering applications. Furthermore, full-thickness wound healing study performed in rats supported them as a promising wound dressing material.

The third part of the thesis presents the fabrication of chemically cross-linked highly porous SPI cryogels. Herein, glutaraldehyde (GA) cross-linked macroporous sponge-like SPI scaffolds were prepared using the cryogelation technique for tissue engineering

applications. The prepared SPI cryogel scaffolds possess an interconnected porous structure with a high porosity with pore sizes in the range of micrometres. The physicochemical properties of the fabricated scaffolds were analyzed through FTIR, SEM, TGA and DSC. The morphology, porosity, swelling capacity, and degradation rate of the cryogels were found to be dependent on the concentration of polymer to crosslinking agent. All cryogels showed elasticity and physical integrity in cyclic compression analysis, as these matrices restored their original length after being compressed to one-fifth of their original length. These cryogels showed excellent mechanical properties, immediate water-triggered shape restoration and absorption speed. Furthermore, cryogels outperformed cotton and gauze in terms of blood clotting and blood cell adherence. The *in vitro* and *in vivo* studies demonstrated the potency of SPI scaffolds for skin tissue engineering applications. Our findings showed that crosslinking with GA had no detrimental effects on cell viability. In addition, an *in vivo* full-thickness wound healing study in rats validated them as good potential wound dressing materials. Overall, we prepared superporous, non-toxic, stable soy protein cryogels that could be useful in biomedical applications such as cell culture matrices and the replacement of damaged tissue, specifically as a wound dressing.

Besides, in the last part of the thesis we have proposed a platform for topical wound dressing material using a polydimethylsiloxane (PDMS) scaffold in order to enhance the skin healing process. *In vitro* co-culture assessment of epidermal-origin mouse B16-F10 melanocyte cells and mouse L929 fibroblast cells in three-dimensional polymeric scaffolds has been carried out towards developing bio-stable, interconnected, highly macroporous, PDMS based tissue-engineered scaffolds, using the salt leaching method. To determine a suitable ratio of salt to PDMS pre-polymer in the scaffold, two different samples with ratios 2:1 and 3:1 [w/w], were fabricated. Effective pore sizes of both

scaffolds were observed to lie in the desirable range of 152–165  $\mu\text{m}$ . In addition, scaffolds were pre-coated with collagen and investigated as a podium for culturing the chosen cells (fibroblast and melanocyte cells). Experimental results demonstrate not only a high proliferative potential of the skin tissue-specific cells within the fabricated PDMS based scaffolds but also confirm the presence of several other essential attributes such as high interconnectivity, optimum porosity, excellent mechanical strength, gaseous permeability, promising cell compatibility, water absorption capability and desired surface wettability. Therefore, scaffolds facilitate a high degree of cellular adhesion while providing a microenvironment necessary for optimal cellular infiltration and viability. Thus, the outcomes suggest that PDMS based macroporous scaffold can be used as a potential candidate for temporary skin dressing material. In addition, the fabricated PDMS scaffolds may also be exploited for a plethora of other applications in tissue engineering and drug delivery. It can be used as a temporary upper layer in a bilayer skin substitute.

To summarize, the current thesis demonstrates the development and fabrication of a variety of three-dimensional microscale structures by employing the enabling technologies of tissue engineering such as electrospinning, freeze-thawing/cryogelation, and salt-leaching. Overall, the findings of these studies indicate that the developed materials have the potential to be used in the fields of soft tissue engineering and wound healing.

*Keywords:*

*Skin, soy protein isolate, silk fibroin, polyvinyl alcohol, polydimethylsiloxane, electrospinning, freeze-thawing, cryogelation, salt-leaching, tissue engineering, scaffolds, wound dressing.*